Thermomechanical analysis of the wheel-rail contact using a coupled modelling procedure

Naeimi, Meysam; Li, Shaoguang; Li, Zili; Wu, Jun; Petrov, Roumen H.; Sietsma, Jilt; Dollevoet, Rolf

DOI
10.1016/j.triboint.2017.09.010

Publication date
2018

Document Version
Final published version

Published in
Tribology International

Tribology International 117 (2018) 250–260

Contents lists available at ScienceDirect

Tribology International

journal homepage: www.elsevier.com/locate/triboint

Thermomechanical analysis of the wheel-rail contact using a coupled modelling procedure

Meysam Naeimi [a], Shaoguang Li [a], Zili Li [a,*], Jun Wu [b,c], Roumen H. Petrov [b,c], Jilt Sietsma [b,c], Rolf Dollevoet [a]

[a] Section of Railway Engineering, Faculty of Civil Engineering and Geoscience, Delft University of Technology, Delft, The Netherlands
[b] Department of Materials Science and Engineering, Delft University of Technology, Delft, The Netherlands
[c] Department of Materials Science and Engineering, Ghent University, Ghent, Belgium

ARTICLE INFO

Keywords:
Thermomechanical coupling
Temperature
Finite element
Thermal effects
Wheel-rail contact

ABSTRACT

This research presents a coupled thermomechanical modelling procedure for the wheel-rail contact problem and computes the flash-temperature and stress-strain responses when thermal effects are present. A three-dimensional elasto-plastic finite element model was built considering the wheel-track interaction. When the wheel is running on rail, frictional energy is generated and converted into heat. To evaluate the contribution of thermal effects and plasticity, five different material models were studied among them TEPS was nonlinear and temperature-dependent including thermal softening. Discussions were made on the effect of solution type and material type. The rail temperature, calculated for a critical creepage case, confirmed the potential of martensitic phase transformation. Thermal effects were also important at lower creepages, where a synchronization effect causes earlier damage.

1. Introduction

Friction between wheels and rails is an important agent that provides adhesion and traction/braking possibilities for trains. On the other hand, due to friction, part of the mechanical energy is dissipated by the frictional work when the train wheels run along the rail. Most of this frictional work is transformed into the frictional heat between the in-contact surfaces. Due to the small size of the contact patch, this frictional heat can significantly increase the temperature of the adjacent materials. The heating of wheel and rail materials can be a critical issue as it may lead to thermomechanical fatigue and/or microstructural transformations [1] e.g. generation of the brittle white etching layer (WEL).

The problem of thermal fatigue in wheels created by thermal loads has been investigated in a number of studies. According to [2,3], the initiation and propagation of surface cracks in wheels are highly related to the presence of thermal loads. An overview of the rolling contact fatigue (RCF) phenomenon in wheels and rails, considering both mechanical and thermal loading by rolling contact, has been published in Ref. [4]. More recently, the fatigue behaviour of railway wheels under combined thermal and mechanical loadings has been studied [5], where thermal effects have created high stresses and decreased the fatigue life of wheel materials.

Temperature rise and thermal stresses are also detrimental to the fatigue life of rails, considering the similar microstructure and loading conditions of the wheels and rails. Numerical simulations in Ref. [6] indicate that thermal loading has a significant influence on plastic strains and residual stresses at the rail surface, which can expedite the formation of RCF cracks.

A classical research about the RCF in the wheel-rail system [7] lists some controllable variables that can influence RCF: the contact forces, the size, geometry and location of the wheel-rail contact patch, the friction forces, lubrication, the residual, bending and thermal stresses and the material properties. In addition to these, the random character of the acting loads, contact geometries and fatigue strength of materials is considered in Ref. [4] as an important aspect in fatigue of railway components. Various models are also available for predicting the fatigue life in the wheel and rail materials, e.g. shear strains fatigue failure, multiaxial fatigue damage and energy-density based models [8].

Thermal effects in the wheel-rail contact can affect the magnitude and distribution of residual stress and strain components [9], altering the shakedown behaviour and fatigue life of materials. When the elastic limit of the material is exceeded, plastic deformations occur and after the load

* Corresponding author.
E-mail addresses: m.naeimi@tudelft.nl (M. Naeimi), Z.Li@tudelft.nl (Z. Li).

https://doi.org/10.1016/j.triboint.2017.09.010
Received 26 July 2017; Received in revised form 10 September 2017; Accepted 11 September 2017
Available online 14 September 2017

removal, residual stresses remain in materials [9]. Thermal stresses due to frictional heating can have additional contribution to the total stresses. According to [9,10], if thermal stresses in the sliding wheel-rail contact are superimposed on the mechanical contact stresses, the elastic and shakedown limits of the wheel and rail will be reduced, and yielding will begin at lower mechanical loads. These thermal stresses are generated in a very thin surface layer of materials in contact where elevated temperature occurs [10].

Another potential problem is that the contact temperatures might be high enough to cause thermally-induced phase transformation in wheel-rail materials. According to a recent study [11], evidence of severe thermal loading and WEL formation is often associated with rail defects. This phenomenon might also explain the formation of some squat defects. Squats are one of the major RCF defects that occur mostly in the running band of rails and can create high dynamic forces. The contact temperature and thermal stresses could be driving factors for squats initiation. To distinguish thermal origins of such defects, a different name "studs" has even been suggested [12]. By investigating the rail microstructure [13], squats were found to be associated with WEL formation on the surface. When WEL is characterised as martensite microstructure, e.g. Ref. [14], it indicates a temperature rise up to the austenitizing temperature, e.g. 727 °C for the binary Fe- 0.76C steel. In such case, the austenite transforms to martensite during the subsequent rapid cooling. It is also believed that such thermal transformation in rail materials can be linked to high thermal stresses, that may assist WEL formation or even produce it [15]. A recent study in this field [16] relates the formation of WEL to the temperature rise up to austenitization limit.

To deal with the thermal aspects of RCF in rails, a realistic estimate of the thermal stresses and contact temperature is required. A review of the literature shows a general lack of modelling tools for thermomechanical modelling of the wheel-rail contact; see the literature gap and the importance of coupled modelling in the next section. This research develops a coupled thermomechanical tool, capable of simultaneously calculating the flash temperature and stress-strain responses in the wheel-rail materials. It considers detailed material aspects, i.e. temperature-dependency, nonlinearity and thermal softening by importing the material parameters as a function of temperature in the numerical process. The outputs are used to evaluate the influence of thermal effects on stress-strain responses and to predict the potential of WEL formation in the rail.

2. Thermomechanical modelling of the wheel-rail contact

As mentioned above, friction creates heat at the contact interface due to the work done by moving wheels. Frictional behaviours have been studied in many wheel-rail contact models in the literature, dealing with microslip, tangential stresses and deformations. Microslip, which is the relative motion of contact particles, is the origin of many issues like fatigue and wear of wheels and rails. Tangential forces, produced by driving/braking wheels, can significantly change the contact stresses and fatigue behaviours. The numerical models of [17–19] have focused mainly on the tangential problem, surface shear stresses and microslip in the wheel-rail contact, whereas, they have not studied the frictional heat, temperature rise and accompanying thermal stresses.

A growing body of literature has recognised the importance of thermal effects in wheel-rail rolling contact. Some classical studies, e.g. Refs. [20,21], used analytical methods to calculate the temperature rise during sliding contact situations. These studies had the following limitations: 1) They were developed based on the Hertz theory, which is only valid for the contact between elastic materials. Therefore, they cannot consider nonlinear material properties, which is more realistic in the case of wheel-rail contact. 2) They do not consider a wheel in the calculation; instead, they simplify the presence of the wheel with a moving load and heat over the rail surface. 3) They can only deal with the full-slip contact (when the wheel is in complete sliding). Hence, they cannot calculate the temperature rise and thermal stresses under partial-slip conditions. 4) They assume a rigid body creepage on the entire contact patch and they ignore the distribution of microslip at the contact patch, which is typical of railway operation. 5) The material properties and the coefficient of friction were considered independent of the temperature which is not the real case for wheel-rail materials. The mentioned limitations cause inaccuracies in calculating the temperature rise especially at higher temperatures ($T > 300$ °C).

Some researchers calculated the thermal stresses associated with the temperature rise in frictional contact between wheels and rails; see e.g. Refs. [22,23]. A two-dimensional finite element model of the rail has been constructed in Ref. [24], in order to calculate contact temperature, thermal stresses, plastic strains and wear rates of rails. Another 2D finite element model is used in Ref. [6] to investigate the thermal-elastic–-plastic deformations and residual stresses during wheel sliding. A recent study [25] used a 3D finite element model for the rail to determine the temperature rise, residual stresses and plastic strains. Although this 3D model [25] is developed to estimate the temperature rise and thermal stresses, it does not still consider the transformation of the frictional energy at the contact patch into heat. Similar to other studies, it has employed a moving heat source on the rail, by which, the thermal solution has been obtained uncoupled from the mechanical solution.

Looking at the literature, one can see a general lack of a finite element model that simulates the coupled thermomechanical behaviour of the wheel-rail system. By coupled modelling, we mean a model that simultaneously considers: 1) the frictional rolling contact of the wheel and the rail; 2) conversion of the frictional energy at the contact patch into heat; 3) distribution of the generated heat in the upper and lower bodies i.e. the wheel and rail; and 4) simultaneous thermal and mechanical analysis of the wheel-rail contact problem. This coupled behaviour is an important factor for the accurate estimation of the temperature and thermomechanical stresses. The reason is that in a coupled analysis the frictional energy (as a result of the load and microslip) is directly calculated and instantaneously converted into the heat. There is no need to define a simplified heat equation and to apply the thermal flux on a rail surface. The heat source in the coupled model is directly calculated by the product of tangential load and microslip in each element in the contact patch. It provides thus a more realistic condition than considering e.g. an elliptical or uniform heat flow on the surface which was suggested by Ref. [26].

The finite element model of this research simulates the frictional rolling contact process of the wheel over a length of the rail. It provides the following advantages in comparison with the available methods in the literature: 1) in addition to the normal contact problem, this model considers the creepage in the wheel-rail contact, as well as tractive forces, applied to the wheel; 2) the model can simulate both partial-slip and full-sliding contact conditions between the wheel and rail; 3) it considers elasto-plastic material properties with temperature dependency; and 4) by employing a coupled thermomechanical analysis, it directly converts the frictional energy into heat and computes the temperature and thermomechanical stresses.

Fig. 1 shows the finite element model of the wheel-track system developed in this research. The vehicle and the bogie are lumped into mass elements supported by a set of spring-damper elements serving as the primary suspension. The railway track includes the rail, sleepers and, fastening system and ballast. The fastening and the ballast are modelled with their respective parallel spring-damper elements. The spring-dampers between the rail and sleepers (fastening system) provide for the rail a vertical degree of freedom. The sleepers are allowed to move vertically on top of the ballast. The ballast consists of parallel springs and dampers that are at their upper ends connected to the sleepers and at lower ends to the fixed ground. The lateral movement of the wheel is constrained by applying symmetric boundary conditions on it.

This model benefits from a 3D mesh for the wheel, rail and sleepers using 8-node solid elements. To achieve high accuracy with efficient computing time, a non-uniform discretization strategy is used with the finest mesh in the contact region. The elements in the solution zone are

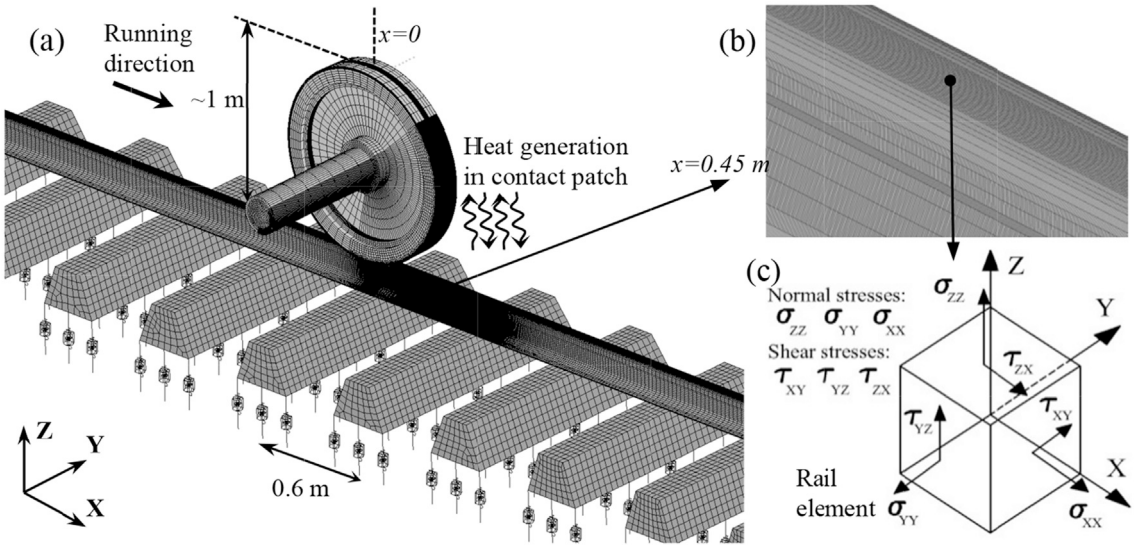

Fig. 1. The finite element model of the wheel on the track system; (a) the finite element mesh; frictional heat is generated in the contact interface; *x=0* is the initial location of the wheel; *x=0.45 m* is the location, at which, the thermomechanical outputs are calculated; (b) magnification of the solution zone in the rail surface, (c) the stress components in one rail element located in the rail surface in the middle of the running band.

refined down to 0.8 mm and the elements far from the solution zone are meshed at an element size up to 7.5 cm. The total number of elements in the model is 1,135,388 and the total number of nodes is 1,297,900. The wheel speed is 38.9 m/s corresponding to the typical Dutch passenger train speed of 140 km/h. The nominal radius of the wheel is 0.46 m and the model length is 20.54 m. At the beginning of simulations ($x = 0$, $t = 0$), stresses and strains are zero and materials are at atmospheric temperature. When the wheel runs over the rail, thermomechanical quantities in materials build up. The outputs of simulations are obtained when the wheel is located at $x = 0.45$ m. The input parameters of the finite element model are given in section 2.2.

2.1. Thermomechanical coupling

The mechanical contact between the wheel and rail is influenced by the heat production and therefore temperature gradients in materials. A suitable computational tool has to be able to consider the contact process as well as the heat conduction. For this kind of problems, thermo-mechanical coupling analysis can be used [27]. To perform a coupling analysis in this research, the finite element modelling consists of two transient problems; see Fig. 2. The finite element model is developed with ANSYS/LS-DYNA, and the coupled thermomechanical problem is solved by LS-DYNA.

2.1.1. Mechanical solver

The mechanical solver is based on Lagrangian formulation for the wheel-rail contact problem. In this solver, an explicit time integration scheme is used due to its stability in achieving accurate solutions with efficient computation [28]. The mechanical part of the analysis is governed by geometric, kinematic and loading parameters applied on the finite element mesh. When the wheel runs over the rail, a surface-to-surface contact scheme based on a master–slave algorithm [29] is used. This activates the underlying frictional algorithm and updates the interface forces and deformations during contact. When the slave node penetrates, an interface force is applied between the slave node and its contact point with the magnitude proportional to the extent of penetration.

According to Coulomb friction law, the limiting friction force

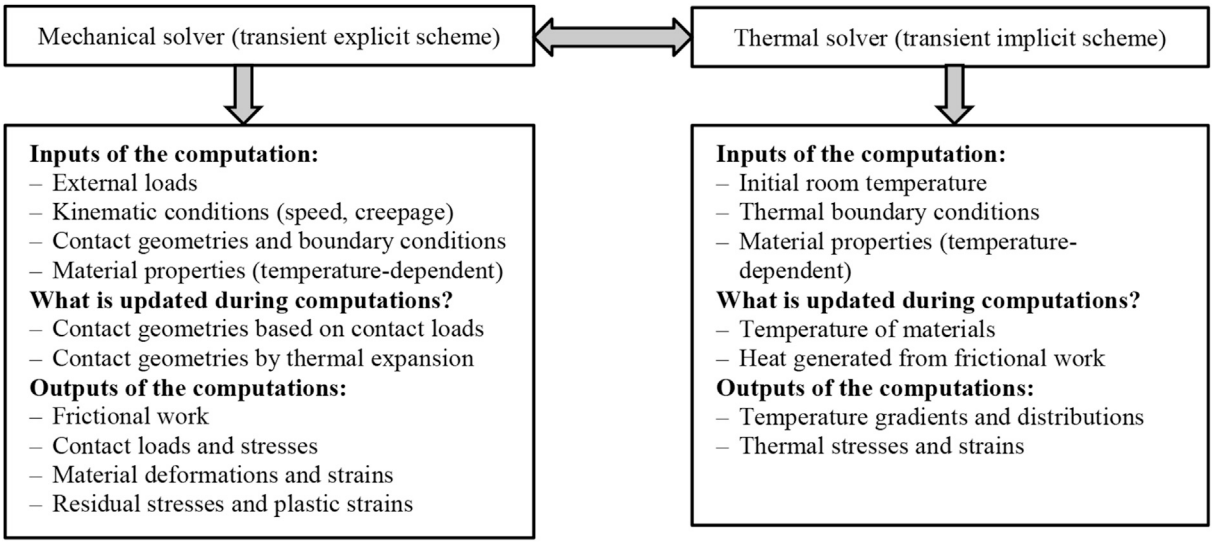

Fig. 2. An overview of the coupled thermomechanical finite element analysis.

between two contact bodies is $f|F_n|$in which, f is the frictional coefficient and $F_n$is the normal contact force. The initial frictional force in the numerical process is [30]:

$$F_f^* = F_f^t - E_f \Delta u_s \tag{1}$$

where, E_f is the interfacial friction modulus, $\Delta u_s$is the incremental tangential displacement during a given time increment and $F_f^t$is the frictional force at time t. The frictional force increment during this time increment is$\Delta F_f = F_f^* - F_f^t$. The stick-slip condition is checked for calculating the evolution of the frictional force in the numerical process. If $F_f^* - f|F_n| \leq 0$ is satisfied, the contact points are in stick and the frictional force at time $t + \Delta t$is calculated as

$$F_f^{t+\Delta t} = F_f^* \tag{2}$$

otherwise ($F_f^* - f|F_n| > 0$), the contact points are in slip and the frictional force at time $t + \Delta t$ is:

$$F_f^{t+\Delta t} = f|F_n| \frac{F_f^*}{\left|F_f^*\right|} \tag{3}$$

The motions of two deformable contact bodies $b_1$and b_2 in the normal (n) and tangential (s) directions are considered. Let $n_1$and $n_2$be the unit normal vectors and $s_1$and s_2 be the unit vectors tangent to the surface of these contact bodies. The impenetrability condition is applied to those portions of these bodies, which are already in contact. It can be written as [31]:

$$v_n^t = v_n^{b1} - v_n^{b2} = \dot{u}_1.n_1 + \dot{u}_2.n_2 \leq 0 \tag{4}$$

where, u_1 and u_2 are the motion vectors, $v_n^{b1}$and v_n^{b2} are the velocity vectors and v_n^t is the relative normal velocity of the two contact bodies. The relative tangential velocity is calculated by:

$$v_s^t = \dot{u}_1.s_1 - \dot{u}_2.s_2 \tag{5}$$

The numerical process uses F_f^t and v_s^tat each time step as the inputs for calculating the frictional energy $\dot{Q}_f^t$ of the contact domain $\Omega$of the two bodies with εas the heat-partitioning factor between these bodies:

$$\dot{Q}_f^t = \int_{\Omega} \varepsilon F_f^t v_s^t ds \tag{6}$$

2.1.2. The thermal solver

The thermal solver in LS-DYNA employs an implicit scheme using a generalized trapezoidal time integration algorithm [32]. The implicit solver is a tailored solver for static and long duration problems. The implicit solver possesses a wider stability region than the explicit method [33], therefore, a larger thermal time step can be taken, which can enhance the calculation efficiency. The time step for the explicit mechanical solver in this research was 4.67×10^{-8} s, which is small enough to meet the Courant stability condition [34], i.e. to ensure that a sound wave may not cross the smallest element during one time step. The time step for the implicit thermal solver in this research was 6×10^{-5} s. This time step is small enough to capture the temperature gradient in the smallest element during the thermal solution as suggested by Ref. [35]. The computational cost of thermal problems (e.g. thermal convection) is far lower when the implicit solver is used. The thermal part of the analysis is controlled by thermal boundary conditions and parameters e.g. specific heat and conductivity. The general heat conduction equation for the given problem can be written by Ref. [36]:

$$\frac{\partial}{\partial x}\left(\lambda_x \frac{\partial T}{\partial x}\right) + \frac{\partial}{\partial y}\left(\lambda_y \frac{\partial T}{\partial y}\right) + \frac{\partial}{\partial z}\left(\lambda_z \frac{\partial T}{\partial z}\right) + I(x,y,z,t) = \rho c \frac{\partial T}{\partial t} \tag{7}$$

where, T is the temperature, ρ is the density, c is the heat capacity, $I(x,y,z,t)$ is the internal heat generation rate per unit volume and $\lambda_x, \lambda_y, \lambda_z$are the thermal conductivity in x, y and z directions. It is a second-order partial differential equation involving rates of change with respect to the time and position. The material points in the contact patch are subjected to the frictional heat $\dot{Q}_f^t$ during the wheel travel. Assuming T_0as the initial temperature, the initial condition will be$T_{x,y,z}^{t=0} = T_0$ and the boundary condition at time t can be written as [37]:

$$\lambda_x \frac{\partial T}{\partial x} n_x + \lambda_y \frac{\partial T}{\partial y} n_y + \lambda_z \frac{\partial T}{\partial z} n_z = \dot{Q}_f^t \tag{8}$$

where, $\lambda_x, \lambda_y, \lambda_z$are the thermal conductivity in x, y and z directions and n_x, n_y, n_z are the normal vectors. There is no closed-form solution available for the aforementioned heat conduction problem. The numerical model of this research solves the aforementioned heat conduction problem by means of a trapezoidal time integration algorithm [32].

In the coupled analysis, the frictional energy in the contact interface ($\dot{Q}_f^t$, which is calculated by the mechanical solver) is first stored as the surface energy density in a temporary file. The numerical tool then considers the frictional energy as the heat source when doing a coupled thermomechanical simulation (Fig. 2). This frictional heat is generated in the upper and lower contact surfaces, i.e., of the wheel and rail. It is immediately conducted in the adjacent wheel-rail materials, resulting in thermal stresses and temperature fields (calculated by the thermal solver).

2.2. Thermomechanical parameters

Mechanical and thermal properties of steel materials are influenced by temperature variations. The thermomechanical model in this research uses the temperature-dependent mechanical and thermal parameters as the input. A bilinear elasto-plastic material model with kinematic hardening is used. Considering the Bauschinger effect, the total stress range in this material model is assumed twice of the initial yield stress [38]. The temperature-dependency of the mechanical parameters is shown in Table 1 and that of the thermal parameters in Table 2. These material parameters are given in Refs. [6,39] for several temperature values in the range of 0–1200 °C. Thermal softening is defined by a reduction of the Young modulus (E), yield strength (σ_y) and hardening modulus (E_p) at elevated temperatures. The rail material with the grade R260Mn has a typical initial yield stress between 452 and 636 MPa [40]. In order to consider the work hardening of the rail material, an enlarged value of yield stress σ_{yref} =800 MPa is used at the initial (room) temperature T_0. The same assumption was also recently made by Refs. [25,28].

In addition to the presented Thermo-elasto-plastic material, a simple elastic model and an elasto-plastic model (independent of temperature) were considered for the sake of comparison. These two material models are called the isothermal materials. For these materials, the properties at the initial temperature (T_0) were used. Numerical simulations were carried out for them using the same finite element model, but with the thermal solver in the coupled analysis being switched off; so that only the mechanical solver was activated.

In total, five material models were defined as listed in Table 3. The TEPS model was the most advanced model considered in this research. The type of numerical solver in each model is also given in Table 3. The mechanical contact solver is used for E and EP and the coupled thermomechanical for ET, TEP and TEPS.

Parameters of the vehicle-track system have significant influences on the numerical results. This research uses the parameters listed in Table 4. Three high creepage scenarios (10, 18 and 26%) were considered for the simulations to account for more critical conditions in terms of heat generation and temperature rise. For the same reason, a high vertical wheel load of 134 kN and a high friction coefficient of 0.6 were selected. The wheel moves with a constant velocity along the rail surface. It also

Table 1
Temperature dependency of mechanical parameters used in the modelling [25,39].

Temperature, T (°C)	Young's modulus, E (GPa)	Poisson's ratio, ν	Yield strength, σ_y (MPa)	Coefficient of thermal expansion, α ($\times 10^{-6}$°C^{-1})	Hardening modulus, E_P (GPa)
24	213	0.295	800.0	9.89	22.7
230	201	0.307	802.1	10.82	26.9
358	193	0.314	735.8	11.15	21.3
452	172	0.32	649.4	11.27	15.6
567	102	0.326	468.1	11.31	6.2
704	50	0.334	362.0	11.28	1.0
900	43	0.345	330.4	11.25	0.1

Table 2
Temperature dependency of thermal parameters used in the modelling [39].

Temperature, T (°C)	Specific heat capacity c (J/kg°C)	Thermal conductivity λ (W/m°C)
0	419.5	59.71
350	629.5	40.88
703	744.5	30.21
704	652.9	30.18
710	653.2	30
800	657.7	25
950	665.2	27.05
1200	677.3	30.46

rotates with a constant rotational velocity in order to create the required creepage given in the table.

3. Results of numerical simulations

Finite element simulations were carried out for the mentioned material models, i.e. E, EP, ET, TEP and TEPS given in Table 3. The results in this section are obtained for the medium creepage scenario ($s = 18\%$).

3.1. Thermomechanical stresses

Fig. 3 shows, for the different models, the time histories of stress components in a rail element in the surface (element number 827,719). Such stresses were recorded for an element located at $x = 0.45$ m (Fig. 1) when the train wheel travels with the given speed along the rail. The abscissa shows the time passed from the moment that wheel has been at its initial location ($x = 0.45$ m). Six stress components are shown, three of which are the orthogonal normal components i.e. the vertical, longitudinal and lateral components. The other three are the shear component in different planes; see the nominations in Fig. 1(c).

As can be seen in Fig. 3, the stresses were zero when there is no wheel around the rail element ($t = 9.6$ ms). The stress components were gradually built up in the chosen element when the wheel gets close to this element (located at $x = 0.45$ m). The stresses reached their maximum when the wheel is nearly on top of this element ($t = 10.1$ ms) and then decreased when the wheel moves away from this element. In the nonlinear models (EP, TEP, TEPS), residual stresses are seen on the right side of the graphs in Fig. 3 ($t = 10.6$ ms), even when the wheel has fully left the solution zone. Two of orthogonal normal stresses ($\sigma_{ZZ}\sigma_{YY}$) were negative (compressive) during the wheel passage, while σ_{XX}revealed a sign reversal because of the loading applied to generate the required creepage ($s = 18\%$). This also caused significant shear stress in the vertical-longitudinal plane (τ_{ZX}). The other shear components (τ_{XY}, τ_{YZ}) were negligible since no lateral load or creepage is considered.

The stress histories of different material models significantly differ in shape and magnitude. To facilitate the comparison, the results of the equivalent von-Mises (V-M) stresses were calculated for the different material models; see Fig. 4(a). The peak stresses, calculated for the different models, are given in Fig. 4(b). The difference in stress between

Table 4
Parameters of the vehicle-track system used in the modelling.

Symbol (units)	Description	Value
F_N (kN)	Vertical load on the wheel	134
V (km/h)	Wheel forward velocity	140
s (%)	Longitudinal creepage	10, 18, 26
V_R (km/h)	Wheel rotational velocity	154, 165, 176
f	Coefficient of friction	0.6
ρ_s (kg/m^3)	Density of wheel-rail material	7850
T_0 (°C)	Initial temperature	25
M_w (kg)	Wheel weight	900
M_s (kg)	Mass of concrete sleeper	280
E_c (GP)	Young's modulus of concrete	38.4
ν_c	Poisson's ratio concrete	0.2
ρ_c (kg/m3)	Density of sleeper material	2520
K_c (kN/m)	Stiffness of primary suspension	880
C_c (N·s/m)	Damping of primary suspension	4000
K_p (kN/m)	Stiffness of rail pad	1,300,000
C_p (N·s/m)	Damping of rail pad	45,000
K_b (kN/m)	Stiffness of ballast	45,000
C_b (N·s/m)	Damping of ballast	32,000

Table 3
The numerical simulations considered in this research.

Number	Type of material model	Model name (abbreviation)	Type of numerical solver	Model description	Type of stress-strain results
1	Elastic (isothermal)	E	Purely mechanical contact (no thermal solution)	It uses linear material properties at T_0 in Table 1. E_P and σ_y were disregarded.	Mechanical loading generates elastic stresses and strains.
2	Elastic-thermal (temperature independent)	ET	Coupled thermomechanical contact	It uses linear material properties at T_0 in Table 1. E_P and σ_y were disregarded. The material is temperature independent.	Mechanical loading generates elastic stresses and strains. Frictional heat generates thermal stresses and strains.
3	Elasto-plastic (isothermal)	EP	Purely mechanical contact (no thermal solution)	It uses bilinear material properties at T_0 including E_P and σ_y.	Mechanical loading generates elastic and residual stresses and strains.
4	Thermo-elasto-plastic (without thermal softening, temperature independent)	TEP	Coupled thermomechanical contact	It uses bilinear material properties at T_0 including E_P and σ_y. The material is temperature independent.	Mechanical loading generates elastic and residual stresses and strains. Frictional heat generates thermal stresses and strains.
5	Thermo-elasto-plastic with thermal softening (temperature dependent)	TEPS	Coupled thermomechanical contact	It uses bilinear material properties at T_0 including E_P and σ_y. Material is temperature-dependent (all parameters in Tables 1 and 2)	Mechanical loading generates elastic and residual stresses and strains. Frictional heat generates thermal stresses and strains.

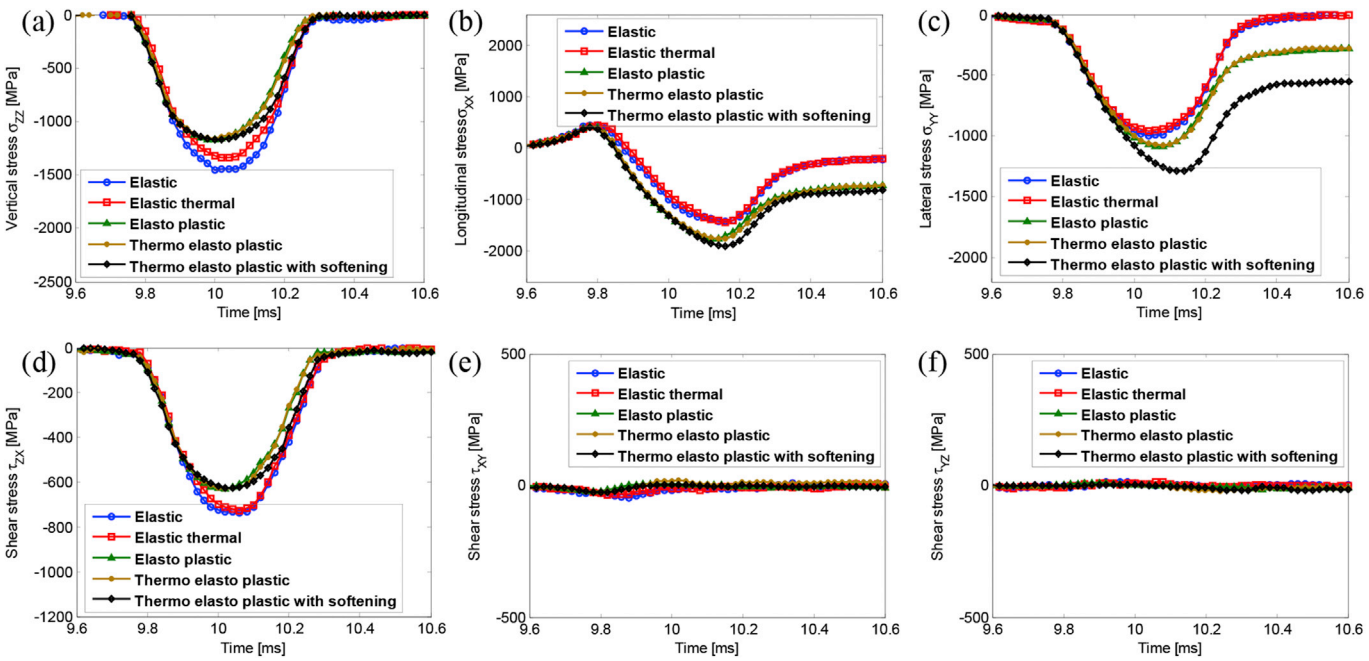

Fig. 3. The stress histories in a rail element at $x = 0.45$ m in the surface for 5 different material models, i.e. Elastic, Elastic thermal, Elasto-plastic, Thermo-elasto-plastic and Thermo-elasto-plastic with softening, (a)σ_{ZZ}; (b)σ_{XX}; (c)σ_{YY}; (d)τ_{ZX}; (e)τ_{XY}; (f).τ_{YZ}.

elastic and plastic models was significant. This is due to the effect of plasticity in materials, which increases the size of the contact patch and reduces the stresses; compare e.g. the σ_{VM}results of E with EP and ET with TEP in Fig. 4. As can be seen in these figures, the peak stresses were higher in the elastic models than in the elasto-plastic models, irrespective of the thermal effects. Another observation is that, in the elastoplastic models, the location of the peak V-M stress shifts forward along the time axis. The abscissa (time) can be interpreted by the wheel location (x) considering the relationship between the speed and time. When the peak V-M stress is shifted forward along the time axis it means that the peak stresses shift towards the trailing edge of the contact patch (x). This is in contrast with the elastic models, in which, the peaks occur nearly in the middle of the contact patch. The reason for this observation is the work hardening and conformity increase between the contact bodies after plastic deformation, which causes the stresses to develop in the location where the maximum plastic deformation occurs [41]. Two of the stress components, i.e. the shear stress $\tau_{ZX}$and the normal stress σ_{YY} are higher at the trailing edge of the contact patch, which creates the same effect on the V-M stresses.

Considering the elastic models (E and ET), it was seen that the thermal effects decrease the magnitude of σ_{VM}. The distribution of σ_{VM} differs more in the nonlinear models (EP, TEP, TEPS), which better indicates the contribution of thermal effects in the stresses. The observation was that the thermal models TEP and TEPS had higher stress peaks than the isothermal model EP. In fact, when thermal effects were introduced, the V-M stresses in the nonlinear models increased.

Fig. 4(b) also provides the results of effective plastic strain left behind in the rail material when the wheel is far enough from the recording point. In the elastic models (E and ET), the strains returned nearly to zero when the wheel is far away and therefore no residual strains were seen. However, in the elasto-plastic models (EP, TEP and TEPS), there were plastic strains in the rail after the loading. According to Fig. 4(b), TEPS produced the greatest plastic strain among different models. The TEPS model also produced the highest peak in σ_{VM} among different nonlinear models. As mentioned, TEPS is the most advanced material model, for which, thermomechanical coupling and the temperature-dependency of materials are considered. These results suggest that when thermal effects are introduced:

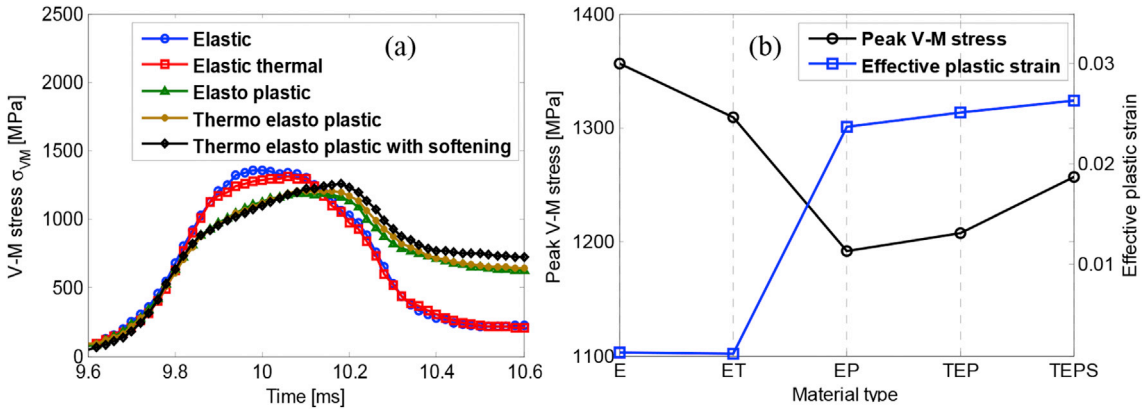

Fig. 4. (a) The history of V-M stress in a rail surface element at $x = 0.45$ m for different material models, i.e. Elastic, Elastic thermal, Elasto-plastic, Thermo-elasto-plastic and Thermo-elasto-plastic with softening; (b) the peak V-M stresses and effective plastic strain in different material models.

- Thermal coupling (the type of analysis) causes higher peak stresses and higher plastic deformations in materials (TEPS vs. EP).
- Thermal softening (the type of material) causes higher peak stresses and higher plastic deformations in materials (TEPS vs. TEP).

The stress distributions in the rail surface obtained for the elastic and elasto-plastic models are in good agreement with those of a former isothermal model in Ref. [41]. In both models (current research and the model of [41]), the peak V-M stress of the elastic solution is higher than that of the elasto-plastic solution. Further, in both models, the peak stress in the elastic solution is shifted towards the trailing edge of the contact patch. The stress results in this research, however, are not quantitatively identical with the results in Ref. [41] as the input parameters were different.

3.2. Temperature results

The flash-temperature during the wheel-rail contact is calculated for the thermal models (ET, TEP and TEPS); apparently, E and EP do not provide thermal outputs. Fig. 5 shows the distribution of flash-temperature in the wheel tread and rail surface during the contact for the medium creepage scenario ($s = 18\%$). The time step $t = 11.52$ ms was selected to obtain the results; at this time step the wheel has already travelled 0.448 m in the longitudinal direction and the thermomechanical outputs are stable. The rolling direction of the wheel is shown with V in the figure. The results for the different material models (ET, TEP and TEPS) are separately presented. The wheel tread temperature in these models is shown in Fig. 5(a, b, c). Fig. 5(d, e, f) show the corresponding rail surface temperature. A magnified view of each temperature distribution around the contact patch is shown in Fig. 5(g, h, i).

To facilitate the comparison, the temperature distributions are plotted along the rail longitudinal axis (x) in Fig. 6 and the peak temperature of the wheel tread and rail surface are listed in Table 5.

According to Figs. 5 and 6, the temperature in the wheel and rail is rapidly increased in the region where contact occurred (a longitudinal distance of around 440 mm $< x <$ 455 mm). The peak occurred near the trailing edge of the contact patch (a longitudinal distance of around 440 mm). This was followed by a fast decay in the opposite side of the running direction ($x <$ 440 mm). There were some local peaks in the decay region because the contact force has fluctuations along the rail as a result of dynamic interaction between the wheel and track system.

According to Table 5, the wheel tread and rail surface had close temperature results since the heat (generated due to friction) is equally distributed between the wheel and rail ($\varepsilon = 0.5$in Eq. (6)). In the TEPS model, a nearly equal temperature (~500 °C) is obtained in the wheel tread and rail surface.

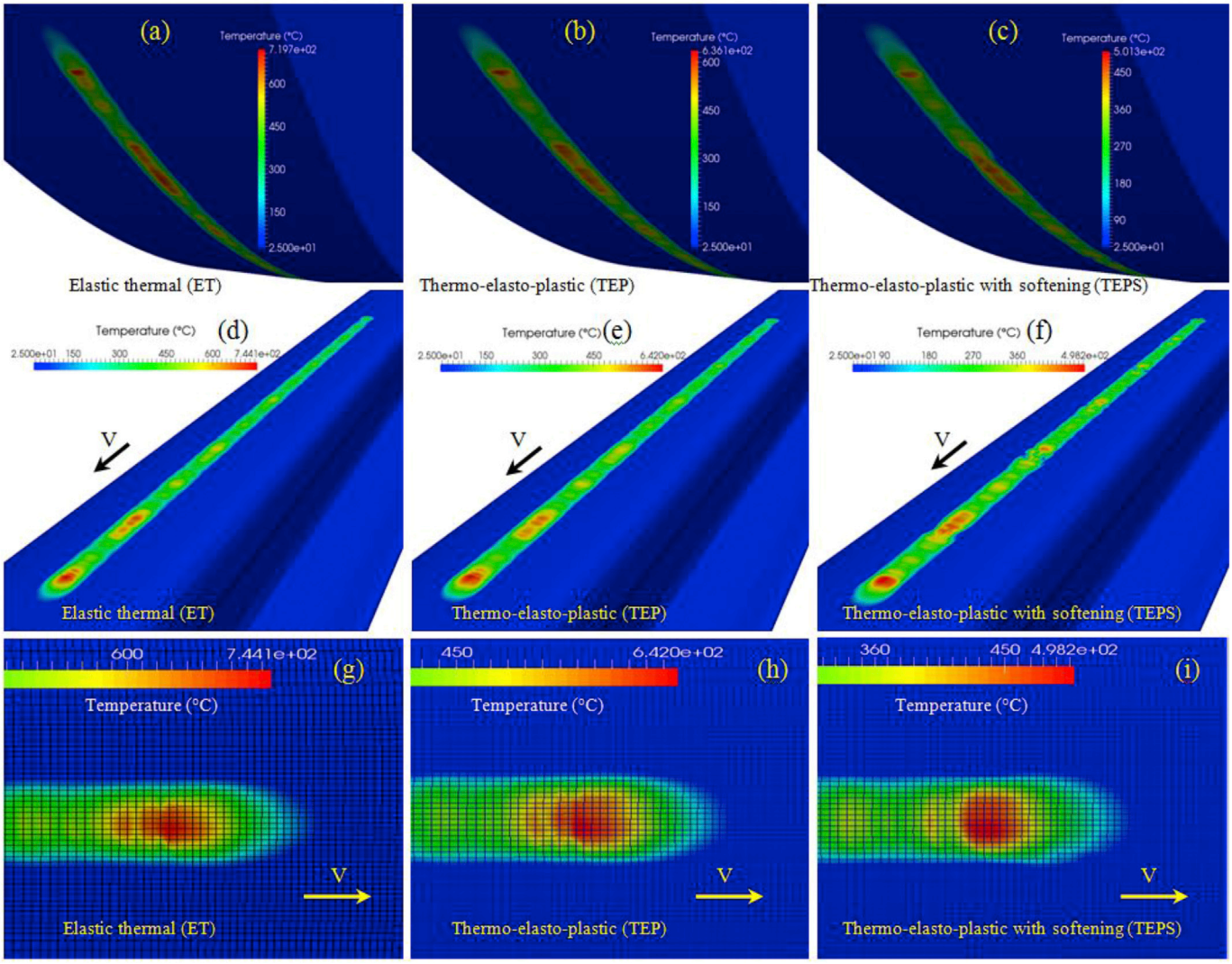

Fig. 5. Temperature distributions in the wheel tread and rail surface under 18% creepage at $t = 11.52$ ms; (a, b, c) wheel tread temperature in ET, TEP and TEPS; (d, e, f) corresponding rail surface temperature in ET, TEP and TEPS; (g, h, i) magnification of the rail surface temperature distribution around the contact patch in ET, TEP and TEPS.

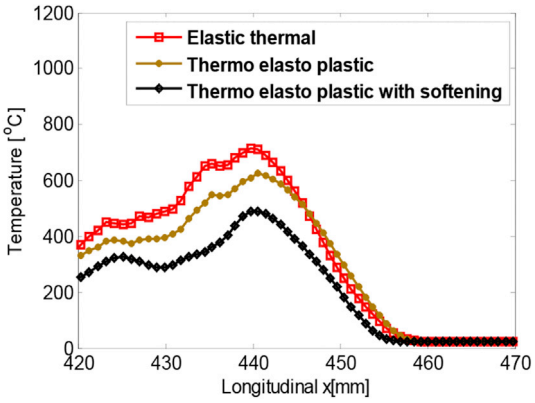

Fig. 6. Temperature distributions in the rail surface along the x axis for different thermal models, i.e. Elastic thermal, Thermo-elasto-plastic and Thermo-elasto-plastic with softening, under 18% creepage.

Table 5
Peak flash-temperature in the wheel and rail for different thermal models under 18% creepage.

Material model	Maximum rail temperature (°C)	Maximum wheel temperature (°C)
ET (Elastic thermal)	744	720
TEP (Thermo-elasto-plastic)	642	636
TEPS (Thermo-elasto-plastic with softening)	498	501

The peak rail temperature for the different material models was different. The maximum rail temperature occurred in the ET model (744 °C). The reason is that ET generates the greatest amount of surface shear stress and microslip. In the elastic model, higher mechanical energy is dissipated in the contact interface by the frictional work, which is proportional to the product of microslip and surface shear stress.

The temperatures in the nonlinear models TEP and TEPS were 642 °C and 498 °C, respectively, which were lower than the elastic model ET. This is because they create lower tangential contact stresses. The other reason is that in the nonlinear models, a fraction of the total energy contributes in forming plastic deformation. Hence, a lower temperature is obtained for TEPS and TEP with the minimum in TEPS (498 °C).

According to section 3.1, among the different nonlinear models, TEPS produced the highest equivalent V-M stress and the highest plastic deformation; and now among the different thermal models, TEPS produced the least flash-temperature.

The temperature distributions obtained in this research are in a reasonable agreement with another FE model in the literature [25]. The general trend, in which, the rail temperature increased in the contact patch with a peak occurring near the trailing edge of the contact patch was also seen in Ref. [25]. The peak temperatures in the current research, however, are not quantitatively identical with those of [25] due to the fact that the FE model in Ref. [25]: 1) includes only the rail and does not simulate the wheel-rail contact problem; 2) is an uncoupled model, in which, the heat source is estimated using theoretical equations; and 3) considers different input parameters.

4. Discussion

4.1. Potential of martensitic transformation at supercritical temperatures

The formation of WEL by the martensitic transformation in rail steel was simulated in a recent study [42], using fast heating and quenching experiments and thermodynamic calculations. Microstructural characteristics of the simulated WEL in these experiments were found to be similar to those observed in the field rail specimens. The experimental results and thermodynamic calculations supported the hypothesis for WEL formation via martensitic transformation [42]. The proposed TEPS model is used to investigate the possibility of temperature rise up to the austenitizing limit. The values of parameters that are given in Tables 1 and 2 for the temperature-dependent elasto-plastic material were used for this purpose. To simulate a more critical situation in terms of frictional heating and its associated temperature rise, a high creepage of 26% was studied, in addition to 10 and 18% given in Table 4. Considering such parameters, the temperature distribution in the rail surface was calculated. Fig. 7 shows the temperature distribution in the rail surface at $t = 11.52$ ms. This result is obtained for the TEPS model under the 26% creepage. A magnified view of the rail temperature around the contact patch is shown in Fig. 7(b). The maximum flash temperature, in this case, was 756 °C.

The results of the three creepage scenarios (10, 18 and 26%) were obtained to investigate the effect of creepage on the stress results and temperature. Fig. 8(a) shows the temperature distributions along the rail under different creepage scenarios. All the results are obtained for TEPS. Fig. 8(b) shows the history of V-M stress in a rail surface element at $x = 0.45$ m. According to Fig. 8(a), the rail temperature is significantly influenced by creepage; the peak temperatures were 284 °C 498 °C and 756 °C for the creepage of 10%, 18% and 26%, respectively. As can be seen in Fig. 8(b), the residual V-M stresses in the rail material were also increased at higher creepages (the trend was less significant than that of temperature). In contrast, creepage had a negligible effect on the peak V-M stresses. These results suggest that a high creepage of 26% increases the flash-temperature (in a significant manner) and residual stresses (to the lower extent), while it has negligible influence on the peak stresses.

Thermodynamic calculations were performed in Ref. [42] to compute the critical phase transformation temperatures. The equilibrium quasi-binary iron-carbon phase diagrams were calculated at atmospheric pressure and at a hydrostatic pressure of 1.8 GPa. According to these calculations, the minimum temperature for austenite to form, Ac_1, is 700 °C at atmospheric pressure. At the hydrostatic pressure of 1.8 GPa, the Ac_1 temperature shifts to 670 °C. These temperature boundaries are superimposed in Fig. 8(a). As shown in this figure, the maximum flash temperature obtained for TEPS with 26% creepage (756 °C) was higher than both the Ac_1 estimated at atmosphere pressure (700 °C) and the one calculated at the hydrostatic pressure of 1.8 GPa (670 °C). This temperature calculation confirms the possibility of forming hard and brittle martensite on the rail surface due to frictional heat in the wheel-rail contact with a high creepage (26% for TEPS). This is also in good agreement with observations made in Ref. [42], where WEL formation by martensitic transformation is simulated in laboratory conditions.

Creepage as high as 26% has been measured in some passenger trains of the Dutch railway and high occurrence of squats have been reported in the railway tracks, for which, these passenger trains being in-service. This indicates that the chosen creepage of 26% and the resulting peak temperature of 756 °C can potentially happen in the Dutch railway.

4.2. Potential of fatigue at subcritical temperatures

Formation of WEL via martensitic phase transformation at supercritical temperatures (above 700 °C as shown in Fig. 8) can reduce the rail lifetime. This is because WEL may promote the initiation of RCF cracks due to the brittle nature of martensite. The close relationship between WEL and RCF cracks has been reported in a number of studies e.g. Ref. [43]. Hence, elevated temperature and formation of WEL can be a possible explanation for RCF initiation.

A creepage as high as 26% is not the typical of railway operation, though it might locally happen in the wheel-rail contact when the trains accelerate or decelerate. Temperature rise and thermal effects can also be important at subcritical temperatures (below 700 °C). Let us consider a more general case of the temperature rise calculated with $s = 18\%$. The rail temperature, in this case, was obtained up to 498 °C, see Fig. 6 and Table 5 (for TEPS which is the most advanced material model). This temperature is lower than the critical phase transformation temperature.

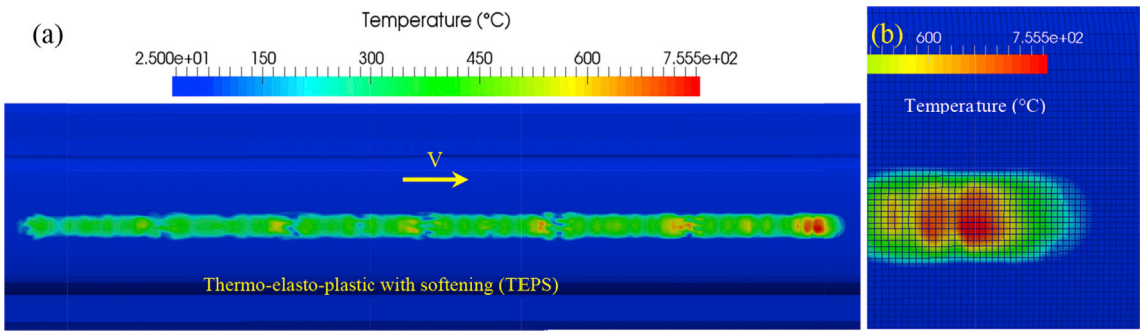

Fig. 7. Distribution of the rail surface temperature at $t = 11.52$ ms; the results are obtained for the TEPS model with 26% creepage; (a) full distribution in the rail top-view; (b) magnification around the contact patch.

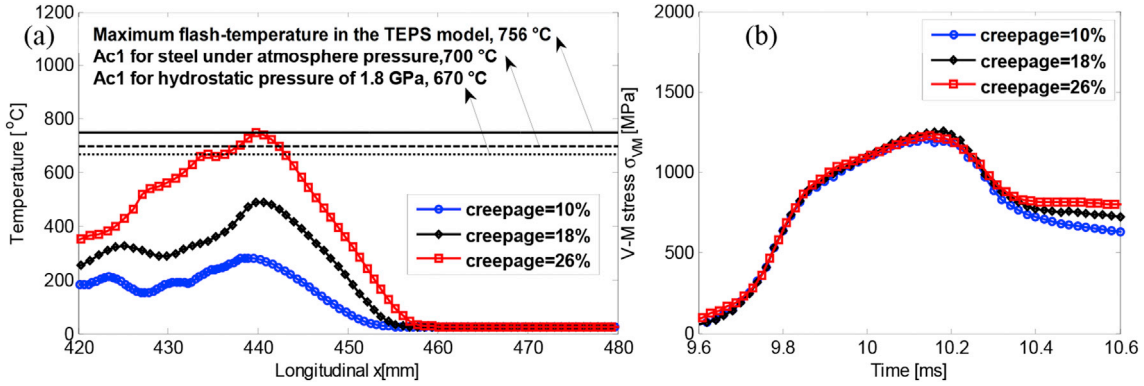

Fig. 8. (a) Temperature distributions in the rail surface along the x axis for TEPS under three different creepage scenarios i.e. 10%, 18% and 26%; (b) history of V-M stress in a rail surface element at $x = 0.45$ m, $y = 0$ with different creepage scenarios.

The evolution of the V-M stresses and strains in the rail during an entire contact cycle is shown in Fig. 9. The results were obtained for all the material models i.e. E, ET, EP, TEP and TEPS. For clarity, the results of thermal and isothermal models are shown separately.

As can be seen in Fig. 9, the magnitudes of effective residual stress and plastic strain in the TEPS model are the greatest among the different models. This is due to the significant thermal effects i.e. the inclusion of thermomechanical coupling and thermal softening (temperature dependency) in the TEPS model.

Without thermal effects (the case of EP), the rail material showed lower plastic strain than the thermal cases, though, the material still had high plastic deformation due to the severe loading considered in this research. When thermal coupling and thermal softening are both involved (the case of TEPS), materials appeared to be less resistant to RCF. Thermal effects, on the one hand, cause a reduction in the elastic and shakedown limits due to thermal softening; see the temperature dependency of $\sigma_y$in Table 1. Therefore, yielding begins at lower stress levels. On the other hand, when thermal stresses are superimposed on the mechanical contact stresses, higher peak and residual stresses and strains were expected (section 3.1). This synchronization effect i.e. the lower yielding limits and higher stresses can lead to earlier RCF damage.

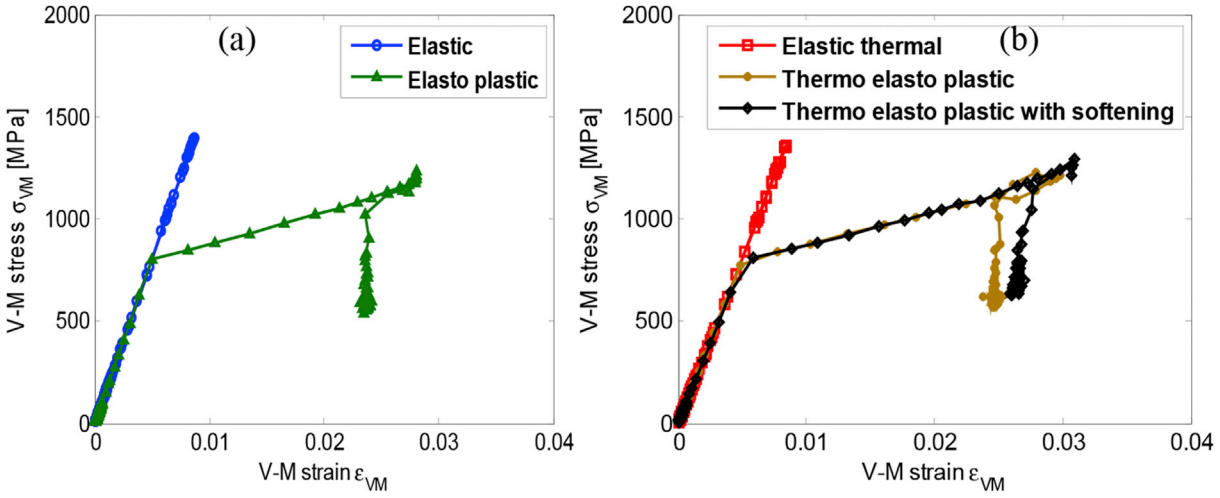

Fig. 9. Evolution of the V-M stresses and strains in a rail element on the surface (number 827,719) for the (a) isothermal material models (Elastic and Elasto-plastic); (b) thermal material models (Elastic thermal, Thermo-elasto-plastic and Thermo-elasto-plastic with softening) during the entire contact cycle with $s = 18\%$.

5. Concluding remarks

To quantify the temperature rise and thermomechanical stresses in the wheel-rail contact problem, a coupled thermomechanical modelling procedure was developed. Different material models with various thermal and mechanical properties were examined. TEPS was the most advanced material model, for which, thermomechanical coupling and temperature-dependency of materials were considered. The numerical model was able to calculate the stresses, deformations and temperatures under various creepage scenarios. Based on the results, the following conclusions are drawn:

1) The comparison between the purely mechanical and the coupled thermomechanical solver revealed that the coupling solver produces higher peak stresses and higher plastic deformations in the rail material. (TEPS vs. EP).
2) The comparison between the temperature-independent and the thermal-softened material revealed that thermal softening causes higher von-Mises stresses and higher plastic deformations in materials (TEPS vs. TEP).
3) Among the different nonlinear material models, TEPS produced the highest equivalent von-Mises stress and the highest plastic deformation. It happened due to the combined effects of thermal softening and thermal coupling, which caused higher thermal stresses. These stresses were superimposed on the mechanical contact stresses and amplified the total stresses.
4) Among the different thermal models, TEPS produced the least flash-temperature (498 °C) in the rail surface. This happened because, in this model, a higher fraction of the total energy contributed to form the high plastic deformation, mentioned in article 4.
5) A nearly equal temperature rise was seen in the contact patch of the wheel and rail since the heat (generated due to friction) was equally distributed between the wheel and rail during the thermomechanical coupling.
6) The temperature distribution in the wheel and rail surface consisted of two regions i.e. a rapid increase in the contact patch and a fast decay in the opposite side of the running direction. The peak occurred near the trailing edge of the contact patch. Some local peaks occurred in the decay region due to contact force fluctuations, caused by dynamic interaction between the wheel and track system.
7) The temperature in the wheel-rail contact was significantly influenced by creepage; for the creepage of 10%, 18% and 26%, the peak temperatures were 284 °C 498 °C and 756 °C, respectively. The higher creepage increased the flash-temperature (in a significant manner) and residual stresses (to the lower extent), while it had negligible influence on the peak von-Mises stresses.
8) The peak temperature in the rail surface calculated for the 26% creepage (756 °C) was sufficient to transform pearlite to austenite. According to equilibrium quasi-binary iron-carbon phase diagrams, the temperature above 700 °C was considered as the supercritical temperature, at which, the potential of WEL formation via martensitic phase transformation was confirmed. Creepage as high as 26% has been measured in some passenger trains of the Dutch railway and high occurrence of squats have been reported in the rails, on which, these passenger trains being in-service.
9) Thermal effects were also important at subcritical temperatures (below 700 °C). Thermal effects, on the one hand, caused a reduction in the elastic and shakedown limits, due to thermal softening. On the other hand, when thermal stresses were superimposed on the mechanical contact stresses, higher stresses and deformations were expected. The results indicated a synchronization effect i.e. the lower yielding limits and higher stresses, which will cause earlier RCF damage.

The high temperature and the mentioned synchronization effect might explain the formation of squat defects. To verify this, further research using thermomechanical modelling and microstructural observations of the defected rails will be needed in future.

Acknowledgment

This research is part of an ExploRail project namely as development of high–performance rail through intelligent metallurgy and engineering (PRIME), in Delft University of Technology. This project (Code: 11247/C38A07) is funded by Dutch rail infra manager ProRail and the Netherlands organization for scientific research (STW/NWO).

References

[1] Ahlström J, Karlsson B. Modelling of heat conduction and phase transformations during sliding of railway wheels. Wear 2002;253:291–300.
[2] Fec M, Utrata D. Elevated temperature fatigue behavior of class B, C and U wheel steels. In: Proceedings of the ASME rail transportation spring conference; 1985. p. 33–9.
[3] Bartley G. A practical view of wheel tread shelling. In: Proceedings of the ninth international wheelset congress; 1988. p. 5.1–5.1.4. Montreal, Canada.
[4] Ekberg A, Kabo E. Fatigue of railway wheels and rails under rolling contact and thermal loading—an overview. Wear 2005;258:1288–300.
[5] Haidari A, Hosseini-Tehrani P. Fatigue analysis of railway wheels under combined thermal and mechanical loads. J Therm Stresses 2014;37:34–50.
[6] Wu L, Wen ZF, Li W, Jin XS. Thermo-elastic-plastic finite element analysis of wheel/rail sliding contact. Wear 2011;271:437–43.
[7] Cannon DF, Pradier H. Rail rolling contact fatigue - research by the European rail research institute. Wear 1996;191:1–13.
[8] Ringsberg JW. Life prediction of rolling contact fatigue crack initiation. Int J fatigue 2001;23:575–86.
[9] Ertz M, Knothe K. Thermal stresses and shakedown in wheel/rail contact. Archive Appl Mech 2003;72:715–29.
[10] Böhmer A, Ertz M, Knothe K. Shakedown limit of rail surfaces including material hardening and thermal stresses. Fatigue & Fract Eng Mater Struct 2003;26:985–98.
[11] Fletcher DI, Sanusi SH. The potential for suppressing rail defect growth through tailoring rail thermo-mechanical properties. Wear 2016;366–367:401–6.
[12] Grassie SL, Fletcher DI, Gallardo Hernandez EA, Summers P. Studs: a squat-type defect in rails. Proc Inst. Mech Eng Part F J Rail Rapid Transit 2012;226:243–56.
[13] Pal S, Valente C, Daniel W, Farjoo M. Metallurgical and physical understanding of rail squat initiation and propagation. Wear 2012;284:30–42.
[14] Zhang H, Ohsaki S, Mitao S, Ohnuma M, Hono K. Microstructural investigation of white etching layer on pearlite steel rail. Mater Sci Eng A 2006;421:191–9.
[15] Baumann G, Fecht H, Liebelt S. Formation of white-etching layers on rail treads. Wear 1996;191:133–40.
[16] Bernsteiner C, Müller G, Meierhofer A, Six K, Künstner D, Dietmaier P. Development of white etching layers on rails: simulations and experiments. Wear 2016;366–367:116–22.
[17] Zhao X, Li Z. The solution of frictional wheel–rail rolling contact with a 3D transient finite element model: validation and error analysis. Wear 2011;271:444–52.
[18] Wei Z, Li Z, Qian Z, Chen R, Dollevoet R. 3D FE modelling and validation of frictional contact with partial slip in compression–shift–rolling evolution. Int J Rail Transp 2016;4:20–36.
[19] Yang Z, Li Z, Dollevoet R. Modelling of non-steady-state transition from single-point to two-point rolling contact. Tribol Int 2016;101:152–63.
[20] Tanvir MA. Temperature rise due to slip between wheel and rail - an analytical solution for hertzian contact. Wear 1980;61:295–308.
[21] Knothe K, Liebelt S. Determination of temperatures for sliding contact with applications for wheel rail systems. Wear 1995;189:91–9.
[22] Fischer FD, Werner E, Yan WY. Thermal stresses for frictional contact in wheel-rail systems. Wear 1997;211:156–63.
[23] Chen WW, Wang QJ. Thermomechanical analysis of elastoplastic bodies in a sliding spherical contact and the effects of sliding speed, heat partition, and thermal softening. J Tribol 2008;130:041402.
[24] Asih AMS, Ding K, Kapoor A. Modelling the effect of steady state wheel temperature on rail wear. Tribol Lett 2013;49:239–49.
[25] Vo KD, Tieu AK, Zhu HT, Kosasih PB. The influence of high temperature due to high adhesion condition on rail damage. Wear 2015;330–331:571–80.
[26] Ertz M, Knothe K. A comparison of analytical and numerical methods for the calculation of temperatures in wheel/rail contact. Wear 2002;253:498–508.
[27] Çaldichoury I, Del Pin F, L'Eplattenier P, Lorenz D, Karajan N. Coupling possibilities in LS-DYNA: development status and sample applications. In: NAFEMS eroupean conference. Frankfurt, Germany: Multiphysics Simulation; 2012. p. 1–44.
[28] Deng X, Qian Z, Dollevoet R. Lagrangian explicit finite element modeling for spin-rolling contact. J Tribol 2015;137:041401.
[29] Hallquist J, Goudreau G, Benson D. Sliding interfaces with contact-impact in large-scale Lagrangian computations. Comput methods Appl Mech Eng 1985;51:107–37.
[30] Zhong Z-H. Finite element procedures for contact-impact problems/Zhi-Hua Zhong. Oxford; New York: Oxford University Press; 1993.
[31] Belytschko T, Liu WK, Moran B. Nonlinear finite elements for continua and structures. Chichester, New York: Wiley; 2000.
[32] LS-DYNA. Thermal analysis user guide. Livermore, USA: Livermore Software Technology Corporation (LSTC Inc.); 1999.

[33] Furuichi M, May DA. Implicit solution of the material transport in Stokes flow simulation: toward thermal convection simulation surrounded by free surface. Comput Phys Commun 2015;192:1–11.
[34] Courant R, Friedrichs K, Lewy H. On the partial difference equations of mathematical physics. Math Ann 1928;11:215–34.
[35] Stout R, Billings PD, Semiconductor P. Accuracy and time resolution in thermal transient finite element analysis. In: ANSYS™ users conference; 2002.
[36] Özõsõk MN. Heat conduction. John Wiley & Sons; 1993.
[37] Hallquist JO. LS-DYNA theory manualvol. 3. Livermore software technology corporation; 2006. p. 25–31.
[38] Bower A, Johnson K. The influence of strain hardening on cumulative plastic deformation in rolling and sliding line contact. J Mech Phys Solids 1989;37:471–93.
[39] Talamini B, Gordon J, Perlman AB. Investigation of the effects of sliding on wheel tread damage. In: ASME 2005 international mechanical engineering congress and exposition. American Society of Mechanical Engineers; 2005. p. 119–25.
[40] Esveld C. Modern railway track. second ed. Zaltbommel, The Netherlands: MTR-Productions; 2001.
[41] Zhao X, Li Z. A three-dimensional finite element solution of frictional wheel–rail rolling contact in elasto-plasticity. Proc Inst. Mech Eng Part J J Eng Tribol 2014;229:86–100.
[42] Wu J, Petrov RH, Naeimi M, Li Z, Dollevoet R, Sietsma J. Laboratory simulation of martensite formation of white etching layer in rail steel. Int J Fatigue 2016;91:11–20.
[43] Clayton P, Allery M. Metallurgical aspects of surface damage problems in rails. Can Metall Quart 1982;21:31–46.